Supplement of Atmos. Meas. Tech., 15, 655–676, 2022
https://doi.org/10.5194/amt-15-655-2022-supplement

Atmospheric Measurement Techniques
Open Access
EGU

Supplement of

Evaluating the PurpleAir monitor as an aerosol light scattering instrument

James R. Ouimette et al.

Correspondence to: James R. Ouimette (jamesouimette@sonomaecologycenter.org)

Supplemental Materials

S1. Instrument description

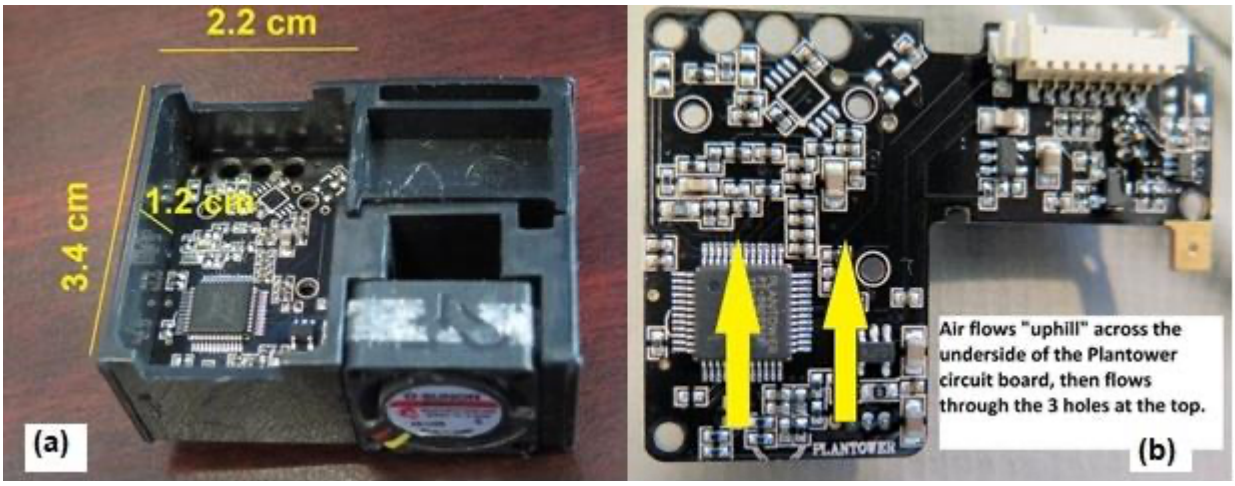

Figure S1. Flow path in the PMS. (a) Location and dimensions of entry chamber on PMS. The fan pulling sample air is located on the lower right of the image. (b) The aerosol flows upward parallel to the circuit board. The air then makes a 180 degree turn through three exit holes to emerge on the other side of the circuit board (the laser and photodiode are located on the back side of the circuit board (not shown) and flows downward through a channel that is illuminated with the laser.

S1.1 Flow rate

The flow rate for the PMS was estimated two ways. The volumetric flow rate was first directly measured to be 14+/-8 $cm^3\ min^{-1}$ at 294 K and 1 atm using a Gilian Gilibrator-2 NIOSH Primary Standard Air Flow Calibrator with a low flow cell. However, it was found that the measured flow rate was very sensitive to backpressure and that the measured flow rate was likely too low.

The flow rate was then estimated by measuring the time it took for a smoke aerosol from a match to be transported and detected by the laser. The transport time average of three runs was 7+/-1 s, as shown in Fig. S2. The volumetric flow rate was then estimated by dividing the PMS total volume between the inlet and the laser by the average transport time. The PMS volume is estimated to be 9.4 + 1.1 = 10.5 cm^3, resulting in an estimated flow rate of 90 $cm^3\ min^{-1}$. This is the value we used in estimating aerosol transport and losses in the PMS. Due to the simplifying assumptions made, this estimate is likely to have an uncertainty of 30%.

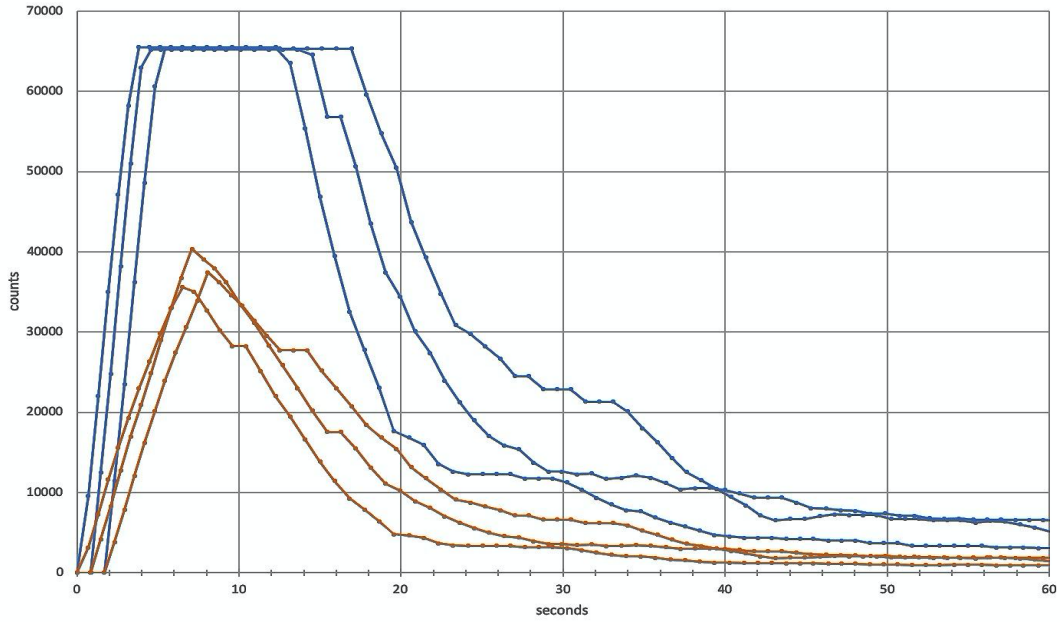

Figure S2. CH1 in blue and CH2 in brown vs. time for a smoke aerosol from a match to be transported and detected by the PMS laser.

S1.2 Aspiration losses to the PMS

Aspiration particle losses are proportional to the particle Stokes number and the ratio of the wind velocity to the inlet face velocity (Hangal and Willeke, 1990):

$$\text{Aspiration efficiency} = 1 - 3 \times \text{Stk}\sqrt{U/Uo} \quad \text{(S1)}$$

valid for $0.003 < \text{Stk} < 0.2$ and $1.25 < U_o/U < 6.25$, where Stk is the particle Stokes number in the wind:

$$Stk = \frac{\rho_p d_p^2 \, U_o}{18\mu D} \quad \text{(S2)}$$

In these equations, U is the sample inlet face velocity, U_o is the wind velocity, d_p^2 is the particle diameter, ρ is the particle density, μ is the air viscosity, and D is the sample inlet diameter. Current literature does not provide data for the PMS face velocity of 5.3 cm s^{-1}, which is much lower than typically used for samplers. As a result, while Eq. S1 shows the importance of increased wind velocity on aspiration losses, the results for PMS may differ from Eq. S1 predictions.

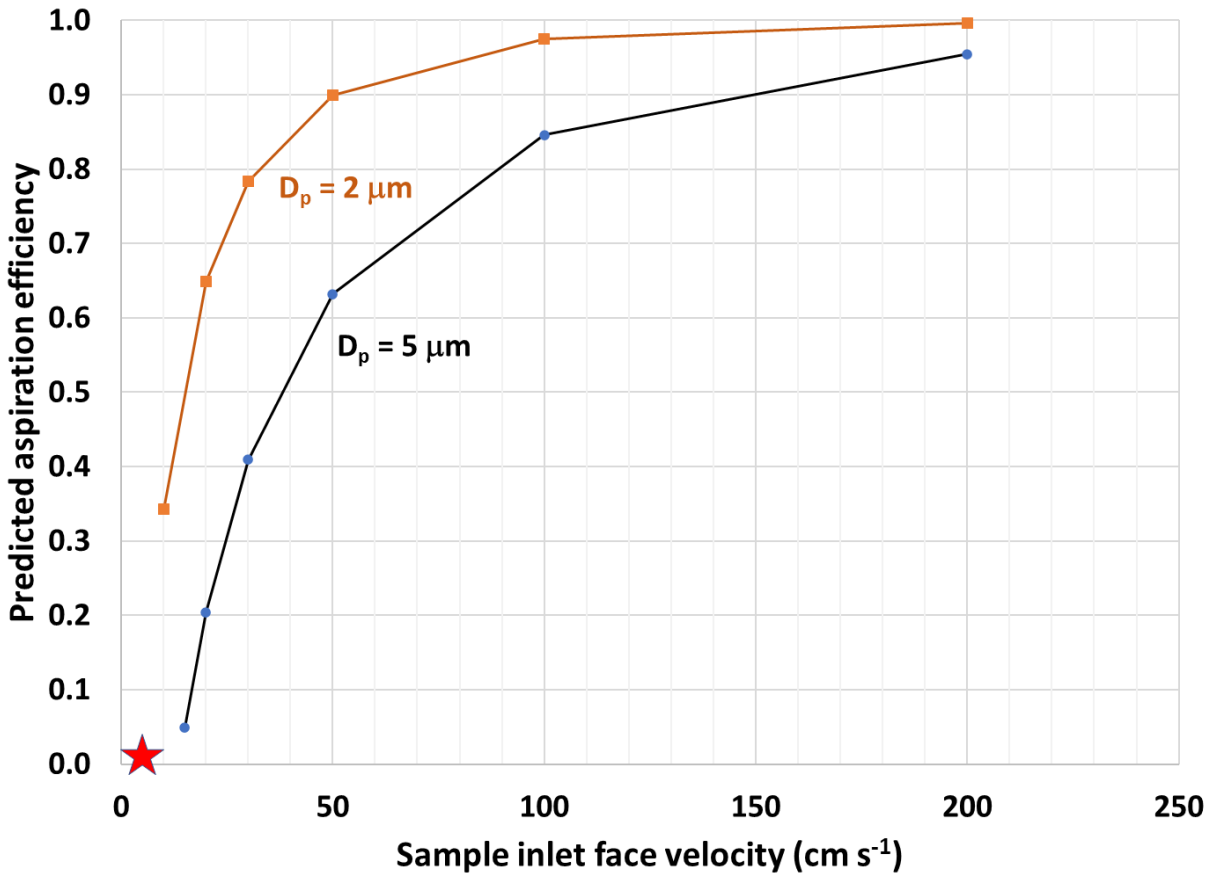

Figure S3. Predicted aspiration efficiency for a downward facing sample inlet using Eq. S1. PMS sample inlet face velocity of 5.3 cm s^{-1} is shown as a red star. Wind velocity is 1 m s^{-1}. Particle density 2 g cm^{-3}. Equation S1 predicts that a lower concentration of larger particles enters the PMS inlet than in the ambient air.

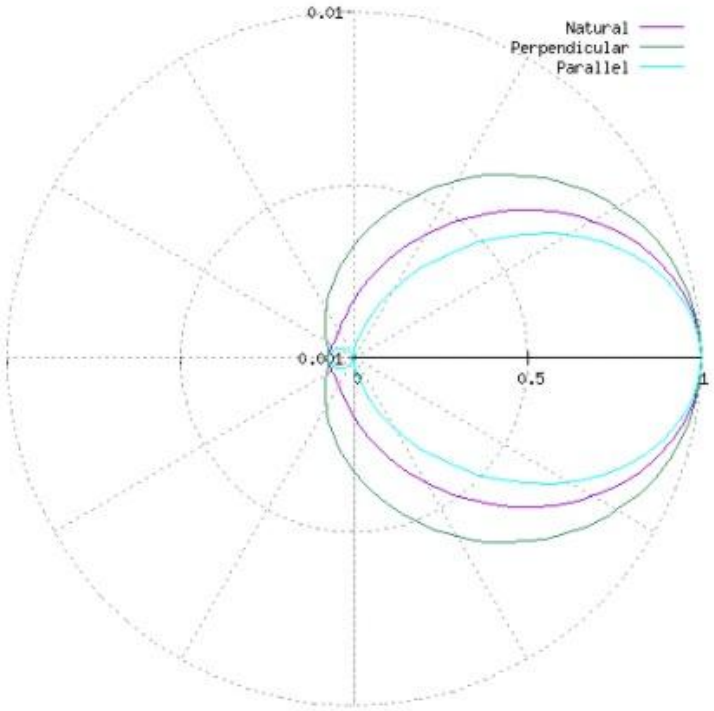

Figure S4. Scattering phase function for 0.3 μm spherical particles of refractive index 1.5 for perpendicular, parallel, and natural polarization at 657 nm. The perpendicular polarization of the scattered light on the photodiode results in significantly higher irradiance from 0.3 μm particles compared to natural or parallel polarization. This would result in higher photodiode current.

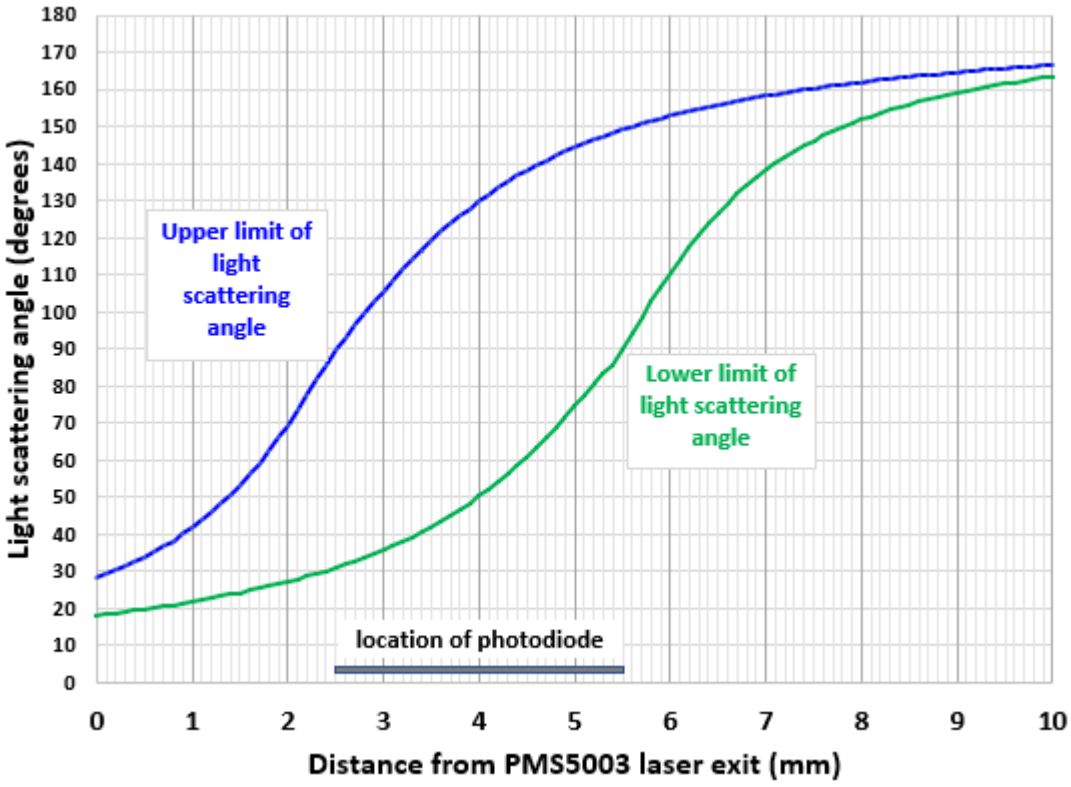

Figure S5. PMS lower and upper angle limits to light scattered from the laser to the photodiode. 1.8 mm from laser to photodiode. Base thickness 0.46 mm.

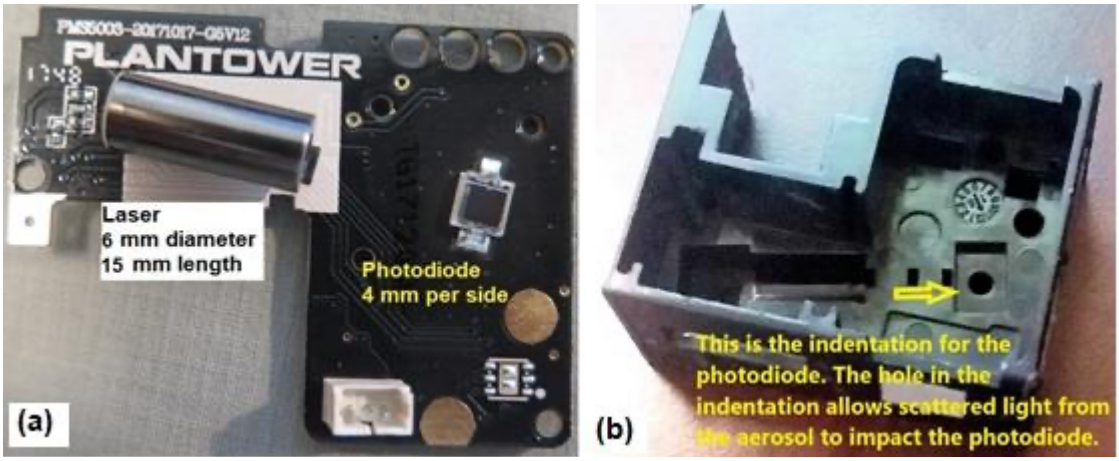

Figure S6. (a) PMS5003 laser and photodiode. (b) Indentation for the photodiode.

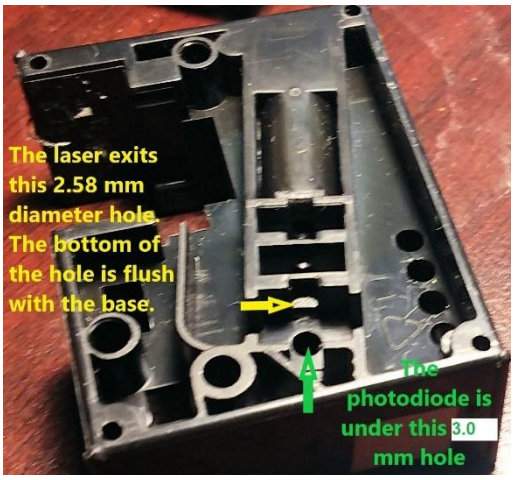

Figure S7. Laser exit hole and photodiode hole.

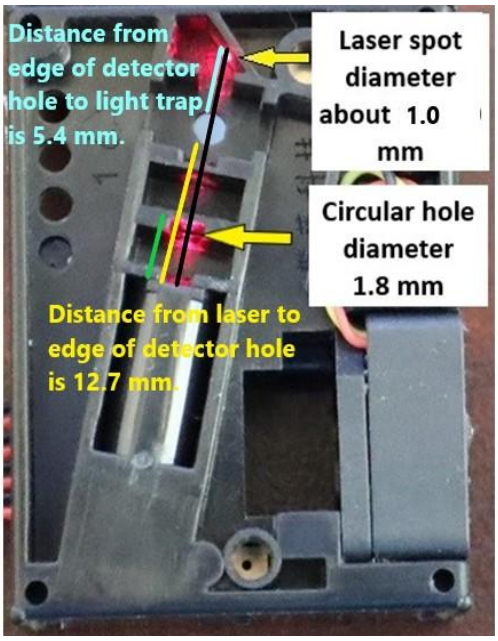

Figure S8. Some dimensions in the PMS5003.

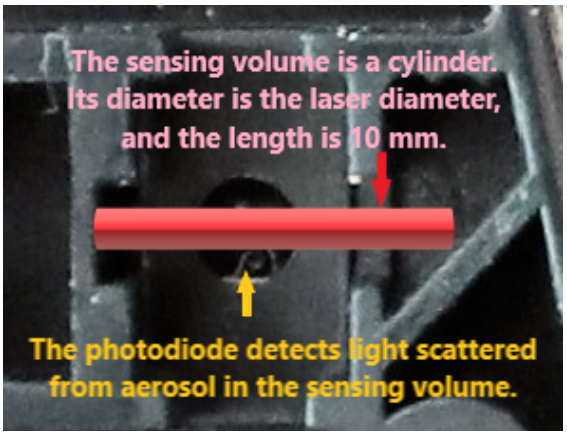

Figure S9. PMS5003 sensing volume.

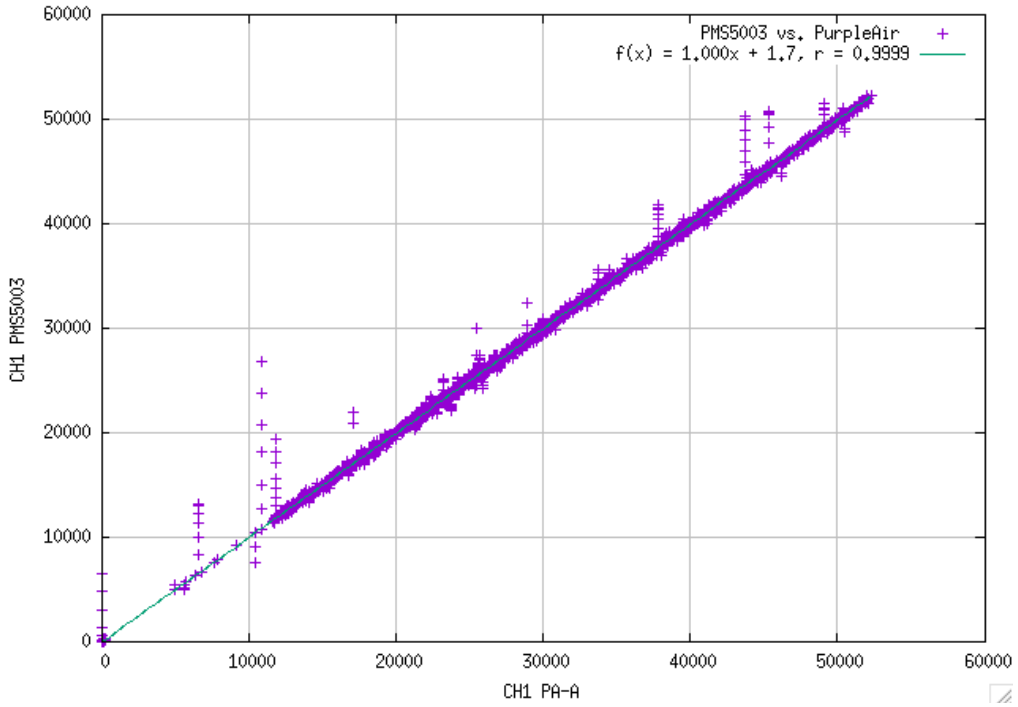

Figure S10. CH1 from PMS5003 vs. CH1 from PA.

S2. CH1 noise when sampling filtered air

There can be significant variation in noise among different PMS units. Table S1 shows the variation we have measured in some of our PMS sensors while sampling filtered air. The PA monitors that were deployed at the Mauna Loa Observatory and Boulder Table Mountain exhibited very low noise when tested on filtered air before deployment.

Table S1. Summary of filtered-air tests of 42 PMS sensors. Sensors in black were acceptable for field use, while sensors in red failed and were not used in the field.

PurpleAir ID	Number of 1-hr averages in filtered air chamber	CH1	
		Sensor A	Sensor B
60:1:94:48:71:e	13	1.15	0.87
80:7d:3a:2b:d8:3f	7	172.00	1.70
80:7d:3a:2b:d9:80 before	6	2.11	1.10
80:7d:3a:2b:d9:80 after Ely NV	72	1.91	0.95
80:7d:3a:2b:e2:24	27	0.36	518.00
80:7d:3a:2f:be:32	9	0.10	0.12
80:7d:3a:51:37:2b	12	0.10	1.46
84:f3:eb:28:d:4d	30	377.00	219.00
84:f3:eb:2a:9f:2c	9	78.20	1.63
84:f3:eb:44:d8:1f	12	35.10	0.25
84:f3:eb:6d:ca:82 before	94	0.42	0.35
84:f3:eb:6d:ca:82 after Boulder City NV	2	0.28	0.15
84:f3:eb:6d:cc:ca	12	0.24	1.84
84:f3:eb:6d:d4:b4	7	0.37	0.33
84:f3:eb:6f:4a:4f	9	0.10	0.38
84:f3:eb:6f:6b:1e	7	20.20	0.12
84:f3:eb:6f:7d:4d	9	0.35	0.30
84:f3:eb:6f:7d:87	17	4.43	8.99
84:f3:eb:6f:7d:8d	5	0.27	0.29
84:f3:eb:7b:c9:e6	6	0.20	26.10
84:f3:eb:7d:7:98	22	3.28	0.26

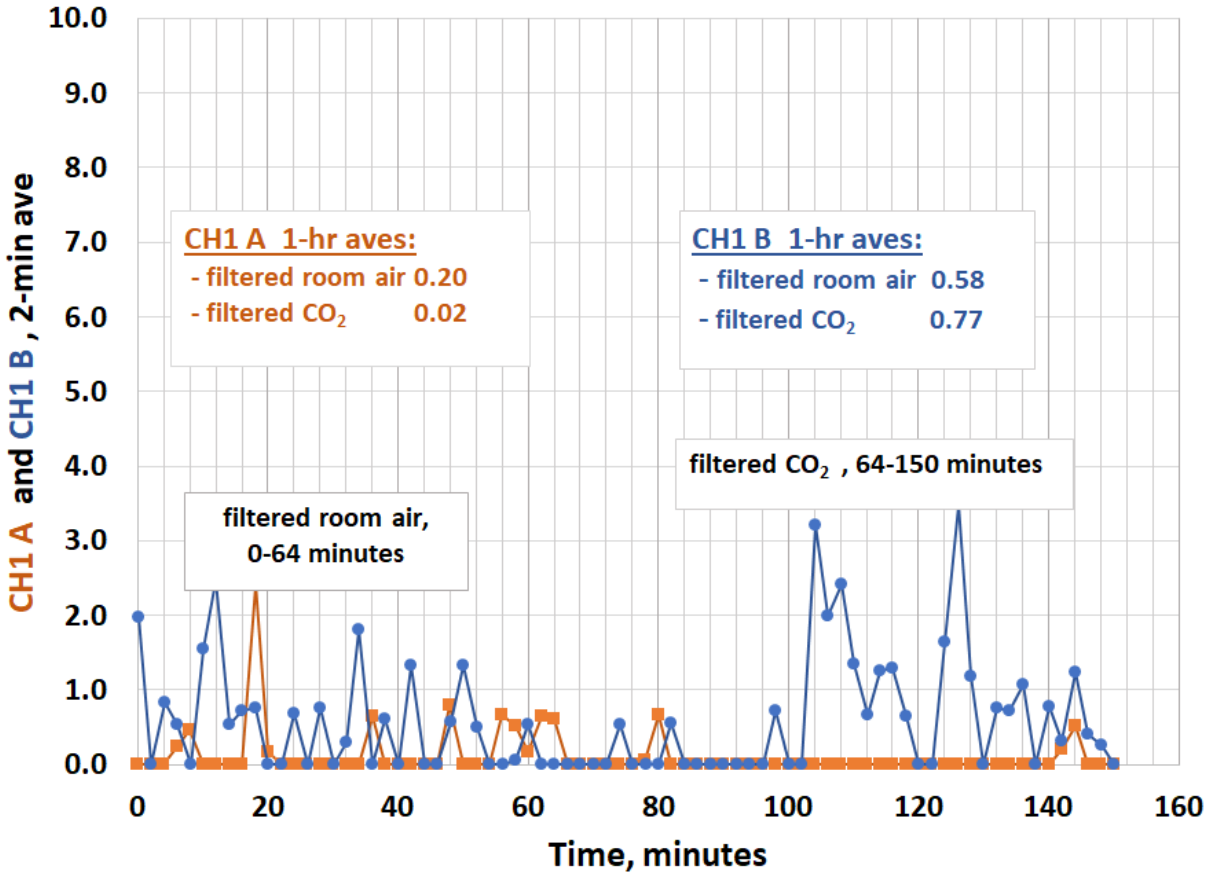

Figure S11. PMS response to filtered air and CO_2. PMS did not respond to air molecules or CO_2.

S3. PMS CH1 and CH1avg precision

The data from the 19 collocated valid PMS sensors in the ten PAs were used to assess the relative variance in the averages between the CH1 and CH1avg. Table S2 presents summary statistics characterizing the variance in the sensors' averages. The CH1A and CH1B statistics were derived from the averages of all data for each PMS sensor, while the CH1avg statistics were calculated by first averaging the data from the two PMS sensors in each PA then averaging these data for each PA. Only nine of the PA units had complete data and were used in the analysis. As shown in Table S2, the coefficient of variation in the average CH1A and CH1B data was 7% and the maximum difference was 28%. The coefficient of variation was reduced to 4.3% for the average CH1avg data, with a maximum difference of 11%. These coefficients of variation are near the precisions of the CH1A and CH1B and CH1avg at high CH1 values, i.e., Un_{mult} in Fig. 2, suggesting that the uncertainty in the CH1 measurements is primarily due to biases between the sensors rather than error in the CH1 measurement itself.

Table S2. Summary statistics on the accuracy in the average PMS sensors and PA monitors. Coefficient of variation is the ratio of the standard deviation and average. Maximum relative difference is the ratio of the difference of the maximum and minimum to minimum average values.

	19 CH1	**9 CH1avg**
Average	1380	1380
Standard Deviation	96.8	59.4
Coefficient of Variation	7.0%	4.3%
Minimum	1212	1326
Maximum	1553	1471
Maximum Relative Difference	28%	11%

To assess the inherent uncertainty of individual CH1 sensors as opposed to uncertainty between sensors, the CH1 values for the different sensors were relatively calibrated by normalizing the values by the sensor average. As shown in Table S1, PA-PMS sensors regularly suffer from large offsets in the CH1 values for filtered air. These offsets in the CH1 data would inflate the additive uncertainty, Un_{add}, in the precision estimates. A clean air test was not conducted for the ten collocated PAs. Potential sensor offsets were evaluated by comparing the lowest values for each sensor. Two sensors had minimum values 2.5 times larger than the median across all sensors, and two others had minimum values 1.5 times larger than the median. These four sensors were removed from the analysis. Figure S12 presents the precision of the CH1 and CH1avg data after normalizing the data by their averages and removing sensors with large offsets. As shown, the uncertainties in the hourly CH1A and CH1B values have been reduced compared to those in Fig. 2 with multiplicative uncertainties of 3% and 1.9% and additive uncertainties of 9 and 6 for CH1A and CH1B and CH1avg, respectively. The minimum detection limits associated with the additive uncertainties are 21 and 14 for the CH1A and CH1B and CH1avg data, respectively.

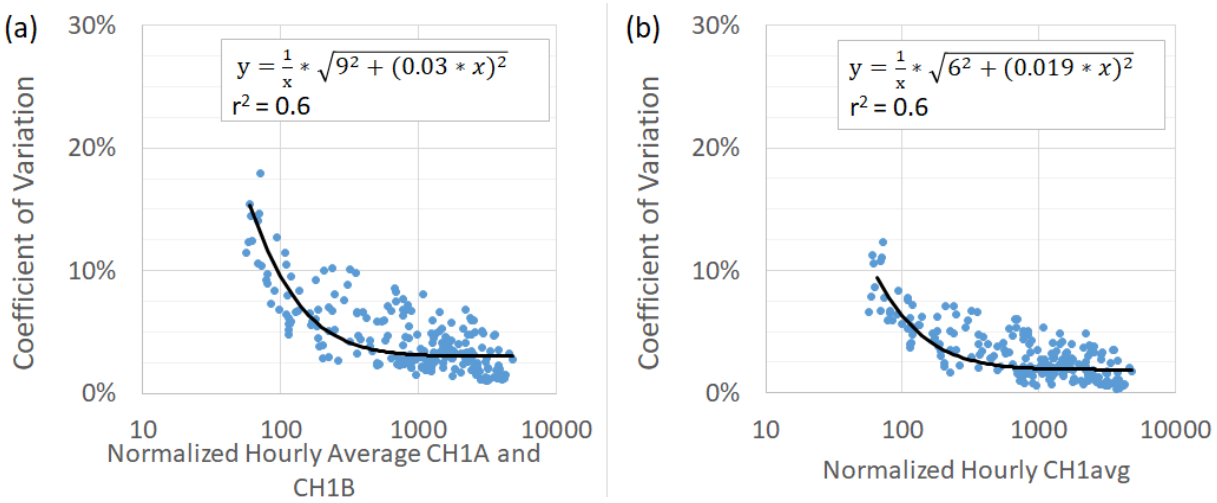

Figure S12. Precision estimated as the coefficient of variation of the hourly CH1A and CH1B (a) and CH1avg values (b). CH1 data were first normalized by their average values, and four PMS sensors were removed from the analysis due to their large offsets as CH1 approached zero.

S4. Effect of PMS geometry on model predictions

Table S3. Effect of uncertainty in measurement of the PMS geometry on model predictions of scattering ratio compared to a perfect nephelometer as a function of particle diameter. The % changes in various dimensions (left most column) are compared to the base case predictions. The base case dimensions are in Sect. 2.2.4, and the base case predictions are on Fig. 7.

Particle diameter (μm)	0.30	0.50	0.70	1.0	2.0	4.0
Scattering ratio for the base case geometry	0.88	0.55	0.38	0.31	0.22	0.23
Change in distance from laser to photodiode (%)	Percent change in scattering ratio compared to base case					
-50	-3	4	26	42	39	26
-25	0	7	20	24	13	15
25	-2	-10	-21	-17	-4	-10
50	-3	-20	-36	-26	-10	-21
Change in diameter of exposed photodiode (%)	Percent change in scattering ratio compared to base case					
-50	-4	-10	-26	-14	-7	-12
-25	-2	-5	-10	-9	-4	-4
25	1	4	8	9	4	5
50	2	6	13	16	8	9
Change in distance of laser exit hole to photodiode (%)	Percent change in scattering ratio compared to base case					
-50	-2	-8	-25	-19	-2	-8
-25	-2	-2	-7	-11	0	-3
25	0	-7	-2	2	-3	-4
50	0	-12	-5	3	-4	-6
Change in thickness of base mask over the photodiode (%)	Percent change in scattering ratio compared to base case					
-50	1	2	1	0	3	1
-25	0	1	1	0	1	1
25	-1	-2	-1	-1	-2	-2
50	-1	-5	-4	-3	-5	-5
Change in distance from photodiode to light trap (%)	Percent change in scattering ratio compared to base case					
-25	3	3	3	3	-2	1
-50	1	1	1	1	-2	0
-75	3	3	3	3	-2	1

S5. Experimental – Field studies

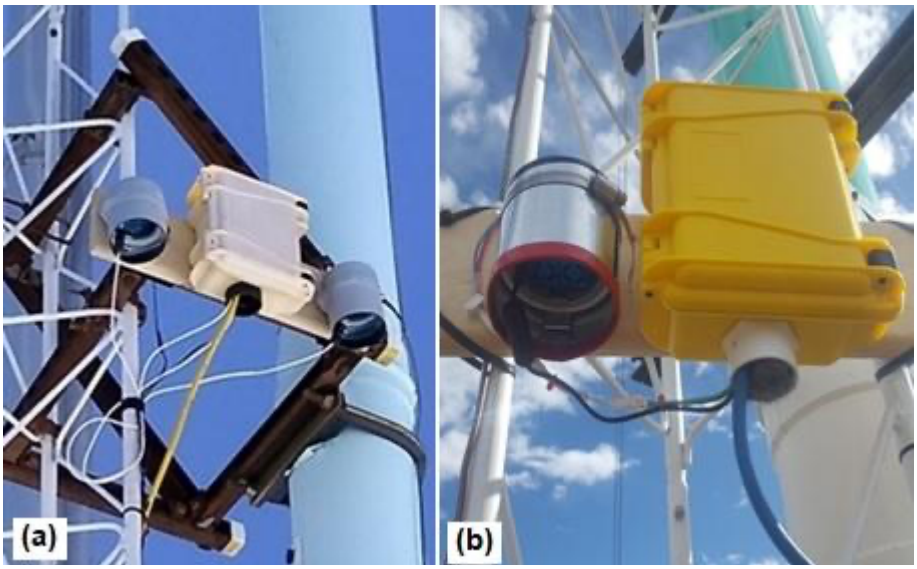

Figure S13. Photos of PA deployments: (a) at MLO - two PAs, one heated and one unheated; (b) at BOS - one heated PA.

S6. Results

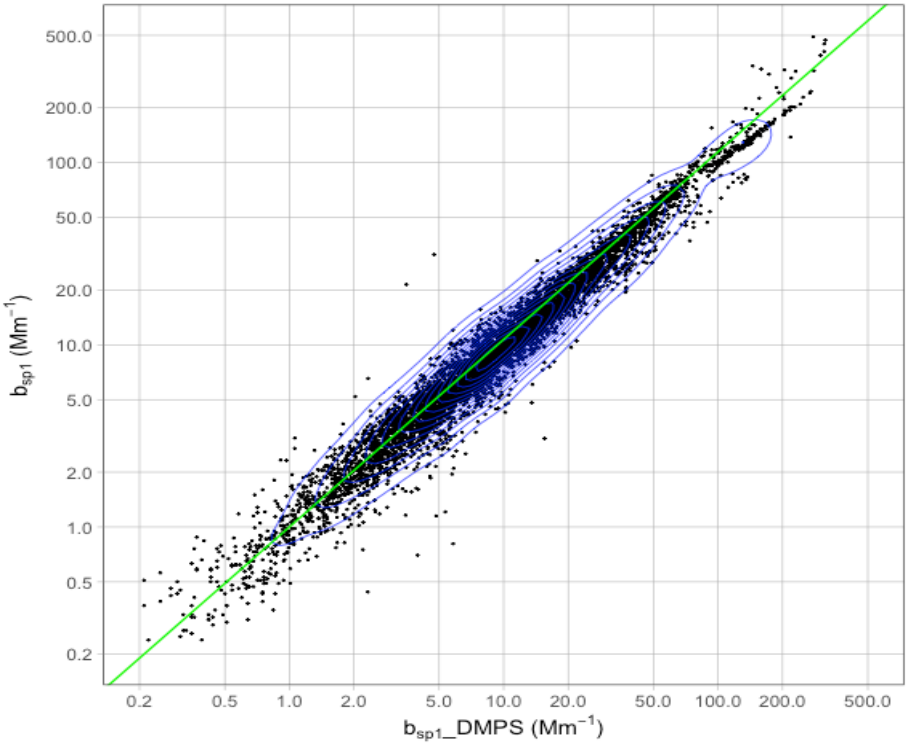

Figure S14. One hour average submicron scattering at 550 nm from nephelometer at BOS vs. scattering calculated from DMPS at BOS, assuming refractive index = 1.53+0.017i. Ninety percent of data are within the outer contour line.

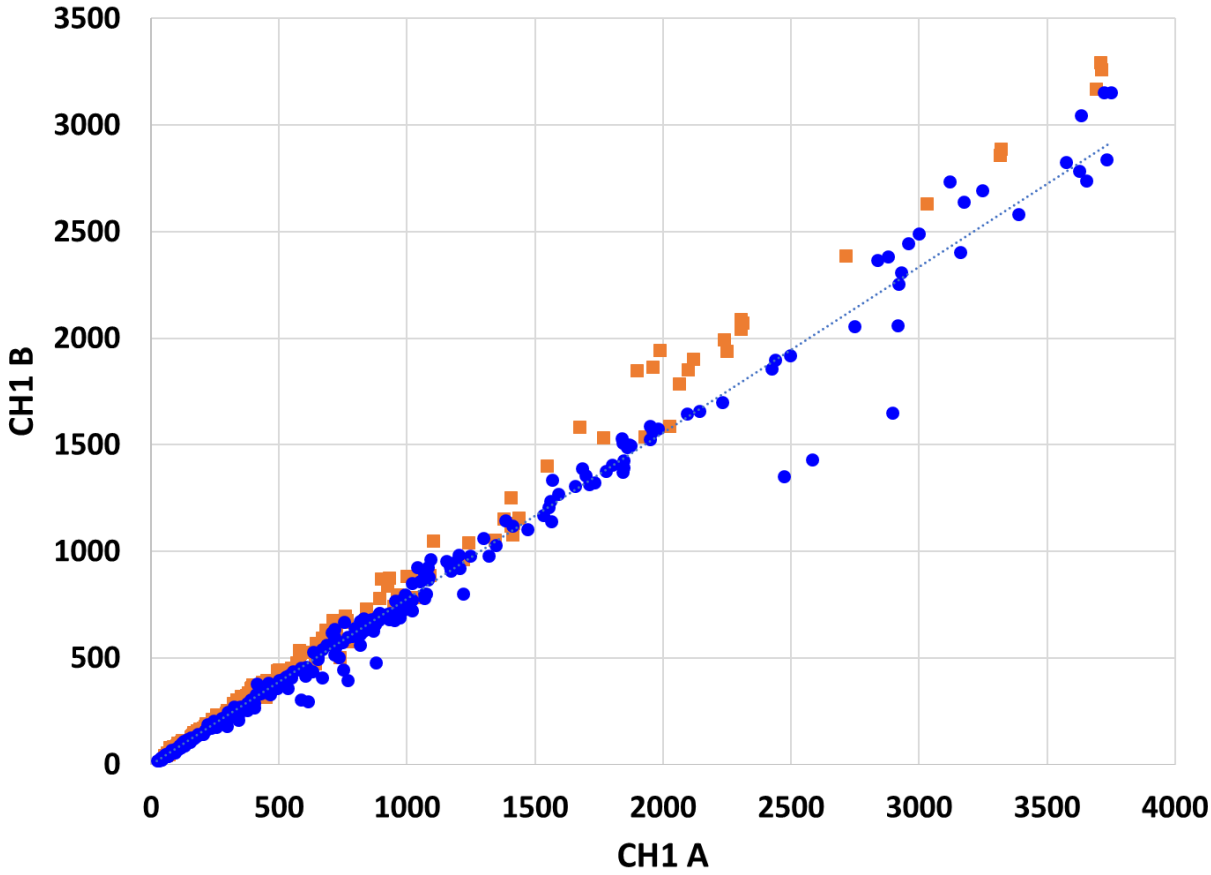

Figure S15. 1 h averages for PMS CH1 sensor A vs. sensor B after one year of service at BOS. Some degradation occurred in CH1B between 7 November 2019 (in orange) and 19 December 2020 (in blue).

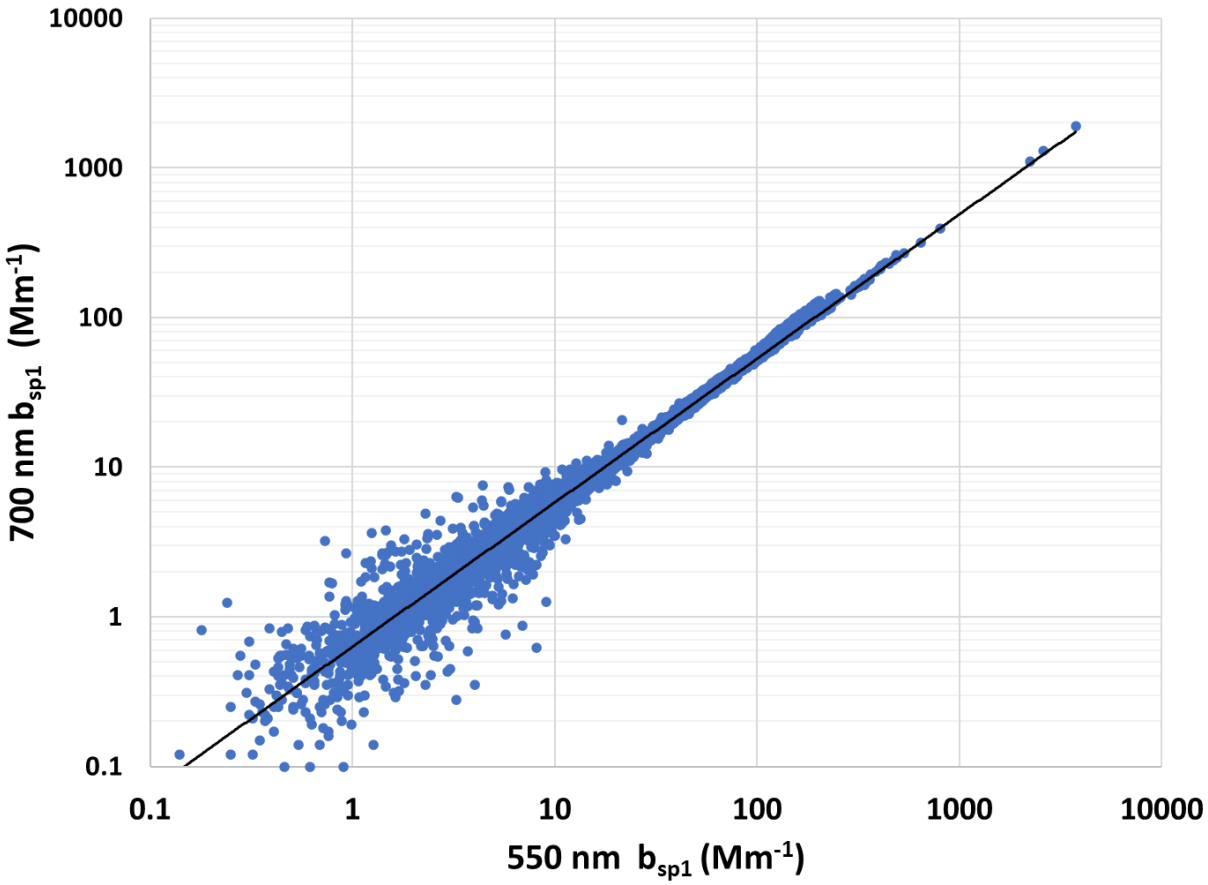

Figure S16. Relationship between submicron aerosol scattering coefficients at 550 nm and 700 nm by TSI 3563. The 700 nm submicron aerosol scattering coefficient averages 52% of the 550 nm submicron aerosol scattering coefficient; 7573 1 h averages, $r^2 = 0.996$. Scattering measurements are from Table Mountain for Feb 2020 to Jan 2021.

The aerosol size distributions from the six size channels of the PMS are also problematic. The MLO and BOS field data show that the other channels are so highly correlated with CH1 that they provide very little additional info (Table S4).

Table S4. Correlation (r^2) of higher channels with CH1 based on MLO and BOS hourly averages (N = 18827 1h averages).

CH1 (>0.3 µm)	CH2 (>0.5 µm)	CH3 (>1.0 µm)	CH4 (>2.5 µm)	CH5 (>5.0 µm)	CH6 (>10 µm)
1.00	0.997	0.90	0.80	0.72	0.71

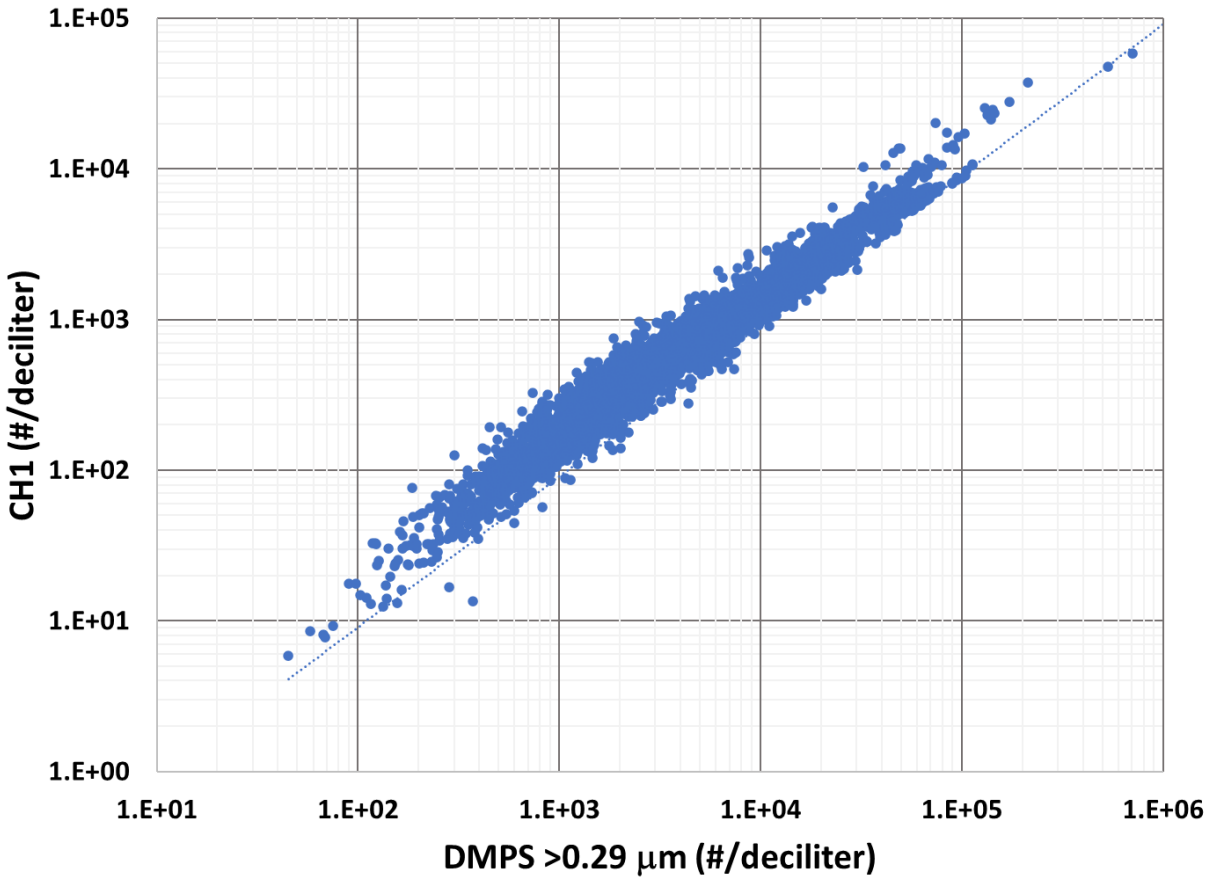

Figure S17. CH1 number concentration averages are a factor of 10 low compared to number concentrations from the DMPS. This shows that CH1 is not an accurate measure of number concentration. Measurements from Table Mountain for February 2020 to November 2020. Plot is based on 5739 1 h averages.

Table S5. PMS normalized size distribution in selected locations throughout the world, from the PurpleAir website. Despite widely varying climates and median concentrations, the PMS creates very similar normalized size distributions. This suggests that the PMS size distributions are created by an unknown algorithm and that they are not accurate.

PMS Normalized Size Distributions in Selected Locations								
Location	Description	Median CH1	Number of 1-hr averages	0.3-0.5µm bin particle # fraction	0.5-1.0µm bin particle # fraction	1.0-2.5µm bin particle # fraction	2.5-5µm bin particle # fraction	5-10µm bin particle # fraction
Mauna Loa Observatory and Table Mtn	This study	100	18,227	0.719 +/- 0.011	0.236 +/- 0.014	0.039 +/- 0.010	0.0050 +/- 0.0038	0.0010 +/- 0.0037
Toolik, Arctic Circle, Alaska	remote cold	142	3,450	0.737 +/- 0.045	0.222 +/- 0.035	0.036 +/- 0.013	0.0031 +/- 0.0041	0.0018 +/- 0.0032
Jeddah, Saudi Arabia	Urban hot desert	4,752	7,768	0.745 +/- 0.032	0.219 +/- 0.026	0.032 +/- 0.009	0.0027 +/- 0.0015	0.0006 +/- 0.0005
Cruzeiro, Amazon, Brazil	High RH jungle	1,028	7,672	0.725 +/- 0.004	0.241 +/- 0.004	0.032 +/- 0.006	0.0013 +/- 0.0006	0.0003 +/- 0.0002
Kumasi, Ghana	Urban	16,011	1,226	0.710 +/- 0.003	0.240 +/- 0.004	0.045 +/- 0.005	0.0041 +/- 0.0010	0.0004 +/- 0.0001
Delhi, India	Urban	15,339	10,553	0.674 +/- 0.001	0.257 +/- 0.016	0.063 +/- 0.015	0.0045 +/- 0.0018	0.0009 +/- 0.0005
Bishkek, Kyrgyzstan	Urban Central Asia	8,269	14,725	0.706 +/- 0.006	0.226 +/- 0.008	0.060 +/- 0.009	0.0058 +/- 0.0017	0.0019 +/- 0.0007
Ulsteinvik, Norway	Cold damp North Sea	449	20,060	0.694 +/- 0.004	0.264 +/- 0.013	0.037 +/- 0.012	0.0025 +/- 0.0030	0.0004 +/- 0.0021
Camp Glenorchy, New Zealand	Remote southern New Zealand	349	4,164	0.718 +/- 0.005	0.235 +/- 0.010	0.040 +/- 0.009	0.0047 +/- 0.0034	0.0009 +/- 0.0019
Sebastopol, California August 12, 2020	wildfire smoke PM2.5 = 183 ug/m3 by BAM	37,514	1	0.696	0.236	0.063	0.0042	0.0005
Keeler, California April 9, 2019	wind-blown dust PM2.5 = 263 ug/m3 by TEOM	3,383	1	0.690	0.167	0.114	0.0199	0.0056

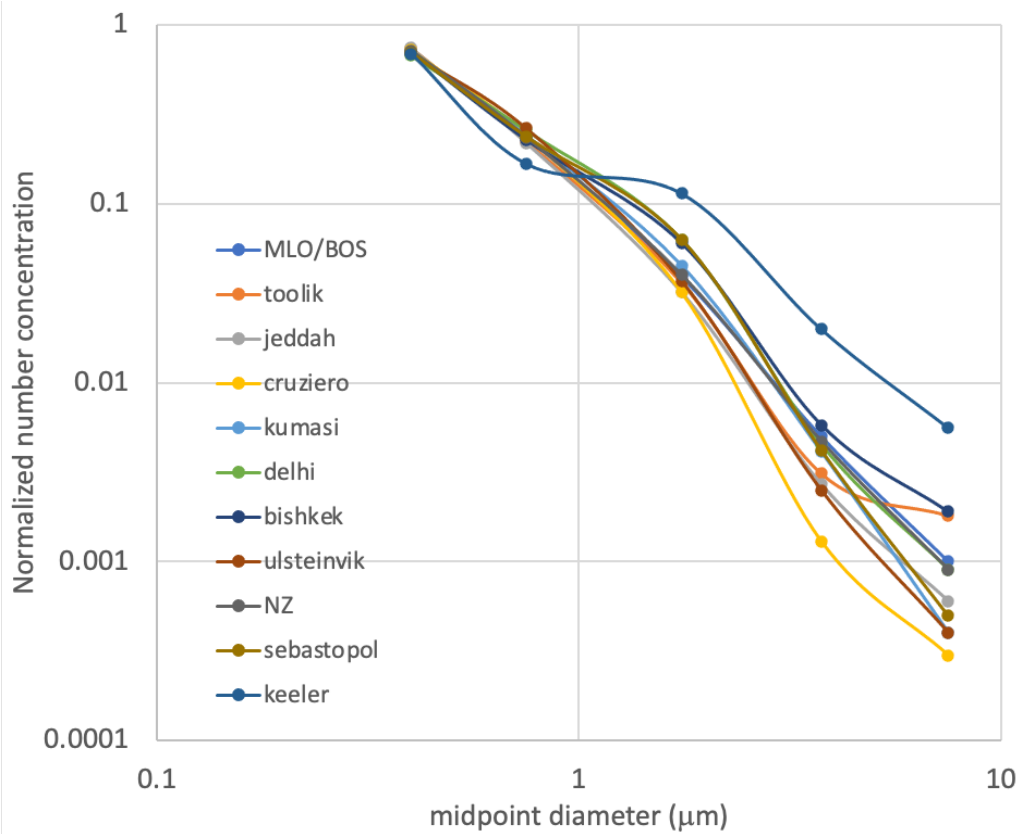

Figure S18. Normalized size distributions from various PMS-PAs based on values in Table S5.

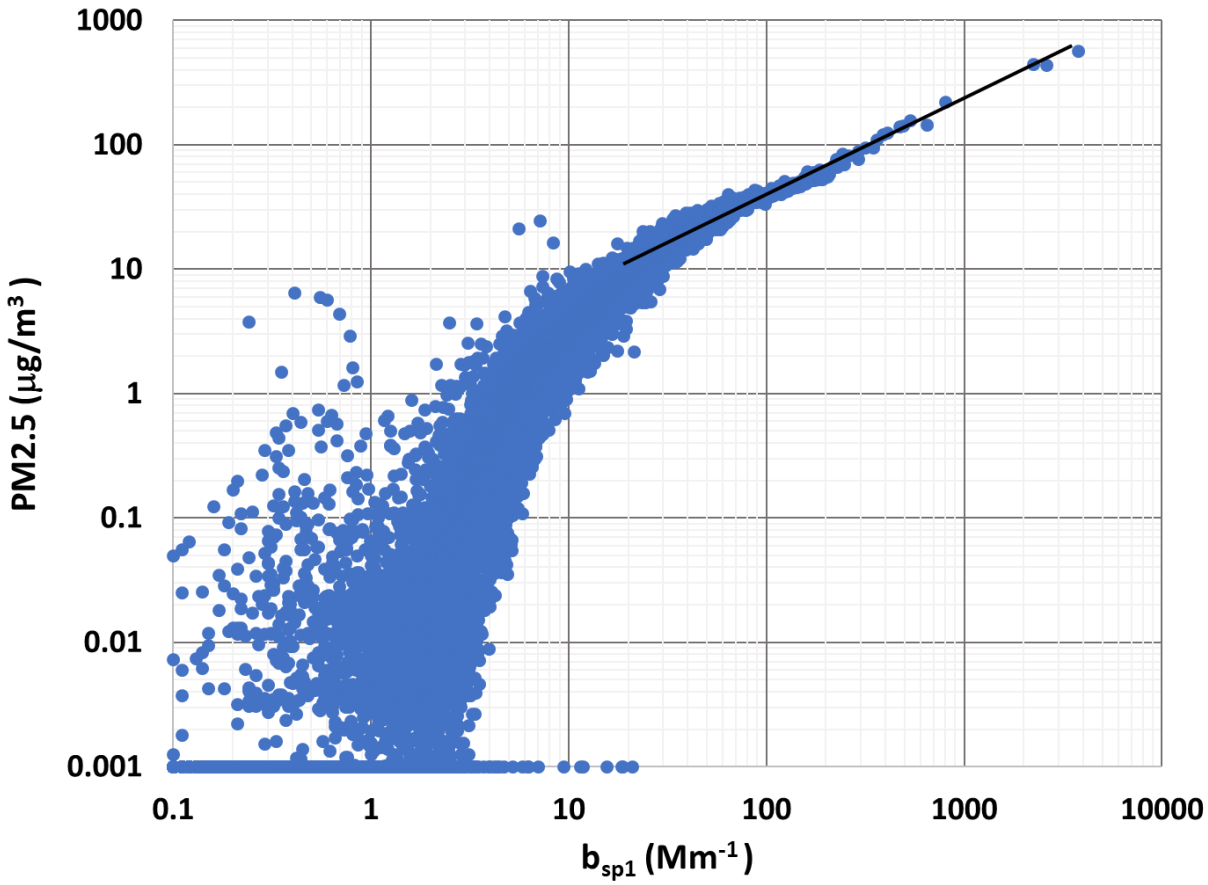

Figure S19. One hour average PA-PMS $PM_{2.5}$_CF1 vs. fine aerosol scattering coefficients from TSI nephelometer b_{sp1}. Total of 14,921 1 h averages from MLO and BOS. Black line is the best linear fit for $PM_{2.5}$ above 10 µg m^{-3}; 6,075 of the $PM_{2.5}$_CF1 values were zero. The zeroes are given a value of 0.001 on this graph.

Table S6. Model-predicted radiant power to the PMS photodiode from a uniform concentration of one particle per cc in the laser sensing volume.

D_p , μm	$\int\int \lvert S_1(\theta,D_p)\rvert^2 \, d\theta \, dx$ λ = 657 nm m = 1.53 - 0.015i	**Radiant power, Watts, from one particle per cc of diameter D_p** (F_0 = 2.3 mW mm^{-2} w = 1 mm, b = 1.5 mm)
0.106	5.69E+00	6.21E-11
0.118	1.08E+01	1.18E-10
0.133	2.22E+01	2.42E-10
0.148	4.19E+01	4.57E-10
0.166	8.24E+01	8.98E-10
0.186	1.59E+02	1.73E-09
0.208	2.96E+02	3.22E-09
0.232	5.25E+02	5.72E-09
0.260	9.10E+02	9.92E-09
0.291	1.49E+03	1.62E-08
0.326	2.35E+03	2.57E-08
0.364	3.63E+03	3.95E-08
0.408	5.21E+03	5.68E-08
0.456	6.71E+03	7.32E-08
0.510	8.99E+03	9.80E-08
0.571	1.26E+04	1.37E-07
0.639	1.46E+04	1.59E-07
0.715	1.71E+04	1.87E-07
0.800	1.99E+04	2.17E-07
0.895	1.96E+04	2.13E-07
1.001	2.24E+04	2.44E-07
1.254	2.59E+04	2.82E-07
1.571	3.30E+04	3.59E-07
1.970	3.76E+04	4.10E-07
2.463	6.77E+04	7.38E-07
3.080	8.22E+04	8.96E-07
3.861	1.07E+05	1.16E-06
4.835	1.41E+05	1.53E-06
6.054	1.88E+05	2.05E-06
7.580	2.46E+05	2.69E-06
9.492	3.26E+05	3.55E-06

References

Hangal, S. and Willeke, K.: Aspiration Efficiency: A unified model for all forward sampling angles, Environ. Sci. Technol., 24, 688-690, DOI 10.1021/es00075a012, 1990.